Journal of Sound and Vibration 392 (2017) 200–216

Contents lists available at ScienceDirect

Journal of Sound and Vibration

journal homepage: www.elsevier.com/locate/jsvi

Broadband liner impedance eduction for multimodal acoustic propagation in the presence of a mean flow

Renata Troian, Didier Dragna*, Christophe Bailly, Marie-Annick Galland

Université de Lyon, École Centrale de Lyon, Laboratoire de Mécanique des Fluides et d'Acoustique (UMR CNRS 5509), 36 avenue Guy de Collongue, 69134 Écully Cedex, France

A R T I C L E I N F O

Article history:
Received 22 December 2015
Received in revised form
3 October 2016
Accepted 10 October 2016
Handling Editor: R.E. Musafir
Available online 18 December 2016

Keywords:
Impedance
Eduction
Multimodal propagation
Time-domain simulation

A B S T R A C T

A new broadband impedance eduction method is introduced to identify the surface impedance of acoustic liners from *in situ* measurements on a test rig. Multimodal acoustic propagation is taken into account in order to reproduce realistic conditions. The present approach is based on the resolution of the linearized 3D Euler equations in the time domain. The broadband impedance time domain boundary condition is prescribed from a multipole impedance model, and is formulated as a differential form well-suited for high-order numerical methods. Numerical values of the model coefficients are determined by minimizing the difference between measured and simulated acoustic quantities, namely the insertion loss and wall pressure fluctuations at a few locations inside the duct. The minimization is performed through a multi-objective optimization thanks to the Non-dominated Sorting Genetic Algorithm-II (NSGA-II). The present eduction method is validated with benchmark data provided by NASA for plane wave propagation, and by synthesized numerical data for multimodal propagation.

1. Introduction

Nacelle manufacturers need to evaluate liner acoustic performance in realistic operating conditions, and inverse techniques are naturally well-suited to identify the impedance properties *in situ*. Only measurements of the sound field properties at selected locations outside the liner region are involved, and furthermore, the liner sample is not destroyed by drilling holes for mounting transducers during these experiments. In order to perform this impedance identification, a numerical model is required for sound propagation in the treated duct, taking account of the presence of a mean flow and of a locally reacting liner. The liner impedance is then estimated by minimizing the error between the calculated and measured sound fields along the duct. Various numerical models for indirect approaches have been proposed, but they have been mostly validated for plane wave propagation. The aim of the present study is to develop an impedance eduction method that can be used for a larger frequency band, in order to consider multimodal acoustic propagation.

The considerable work initiated by Watson et al. [1,2] must be first mentioned. They have developed an impedance eduction method and validated it by comparison with well-documented experiments. A rectangular duct with a ceramic tubular liner section and the presence of a mean flow is considered. The pressure is measured along the duct wall for

* Corresponding author.
E-mail addresses: renata.troian@ec-lyon.fr (R. Troian), didier.dragna@ec-lyon.fr (D. Dragna), christophe.bailly@ec-lyon.fr (C. Bailly), marie-annick.galland@ec-lyon.fr (M.-A. Galland).

http://dx.doi.org/10.1016/j.jsv.2016.10.014
0022-460X/

Nomenclature

A_k, B_k, C_k, Z_∞ coefficient of the multipole model (8)
B half-width of the source (2)
c_0 speed of sound (air)
d liner core depth
f frequency
H Heaviside function
$\mathrm{i} = \sqrt{-1}$ unit imaginary number
I sound intensity
IL insertion loss
$k = \omega/c_0$ wavenumber
L_1,L_2 liner's coordinates on the x-axis
L_x, L_y, L_z length, width and height of the duct
$M = V_b/c_0$ Mach number
n_y, n_z velocity profile parameters
p pressure
P number of real poles in Eq. (8)
Q source term in LEE (1)
S number of complex conjugate pole pairs in Eq. (8)
t time
$\mathbf{v} = (v_x, v_y, v_z)$ velocity
$\mathbf{V_0} = (V_{0x}, V_{0y}, V_{0z})$ mean flow velocity
V_b bulk velocity
W transmitted sound power
$W_{\mathrm{ref}} = 10^{-12}$ W reference sound power
$\mathbf{x} = (x, y, z)$ spatial coordinates
$\mathbf{x_S}$ spatial coordinates of the source
Y surface admittance
Z surface impedance

Greek characters

$\alpha_k \pm \mathrm{i}\beta_k$ complex conjugate pole in Eq. (8)
δ Dirac delta function
Δt, Δx, Δy, Δz temporal and spatial steps
λ_k real pole in Eq. (8)
ρ_0 density (air)
$\omega = 2\pi f$ angular frequency

Subscripts

L lined duct
R rigid duct

Superscripts

$\wedge$ Fourier transform, see Eq. (5)
$\sim$ admittance model coefficient (11)
$*$ complex conjugate

different Mach numbers up to $M=0.4$, frequencies from 500 to 3000 Hz and source levels at 120, 130 and 140 dB. A benchmark database has been created and is still used in numerous studies for validation purposes. Their eduction method is based on the resolution of the convected Helmholtz equation using a finite-element method for computing sound propagation, and pressure measurements on the rigid walls. An analytical mode matching approach has also been used to develop identification methods. In the studies by Elnady et al. [3] and Sellen et al. [4], the duct is divided into three zones (unlined–lined–unlined). The acoustic field in each zone is expanded in terms of the duct eigenmodes, taking into account the associated boundary condition on the duct walls, and is solved by a mode matching method. The minimization process relies on pressure measurements upstream and downstream of the lined section [3]. Mode matching methods offer the advantage of taking high-order modes into account with a competitive computational time, but the convected Helmholtz equation is solved for a simple uniform flow. Richter et al. [5] have developed a time-domain eduction method combining the linearized Euler equations (LEE) and a five parameters extended Helmholtz resonator model for the impedance model. Results have been found significantly improved by taking into account the measured velocity profile in the propagation step. Eversman and Gallman [6] have included an effective mean flow Mach number and the exit impedance of the test channel in the objective function of their eduction process. The inverse method is again performed with a finite-element model. Such extended eduction process improves the impedance identification, in particular for high Mach number flows. Piot et al. [7] and Primus et al. [8] have developed an impedance eduction method which relies on the minimization of the squared error between the acoustic velocity provided by the numerical model and experiments. The linearized Euler equations are solved with a discontinuous Galerkin algorithm, and the acoustic velocity field in a plane perpendicular to the liner surface is measured by laser Doppler anemometry.

All these eduction methods provide good results for plane acoustic waves. However, the acoustic liners are designed for applications involving multimodal propagation, and eduction methods must be generalized to test liners mounted in industrial rigs with more realistic conditions. This is of particular interest for non-locally reacting liners, that cannot be characterized by plane wave at grazing incidence. In the recent work by Watson et al. [9] non-planar waves are considered with multiple higher-order modes in the direction perpendicular to the liner and to the opposite rigid wall. Their eduction process is based on a microphone array mounted on a wall adjacent to the liner. Using measured data in a duct for which several higher-order vertical modes can be separated, the authors have shown that each of these modes is submitted to the same local-reacting impedance at the liner surface. More recently, Buot de l'Epine et al. [10] have investigated a rectangular duct where at least two modes can be cut-on. An eduction method formulated from a Bayesian approach is presented to identify the liner impedance.

In this work, an eduction method suitable for multimodal acoustic propagation is proposed. The difference between measured and simulated insertion loss, together with the wall pressure at a few locations in the duct, is minimized to identify the liner impedance. The linearized Euler equations are solved using a finite-difference time-domain algorithm. A tricky problem in such numerical methods is the frequency impedance boundary condition which must be formulated in the time domain. A comprehensive review of impedance modeling in the time domain can be found in Richter et al. [11]. Among the various available methods, a time-domain implementation based on a recursive convolution algorithm and developed by Reymen et al. [12,13] has been chosen. The three parameter impedance model introduced by Tam and Auriault [14] can be implemented, as well as a broadband impedance model [13,15] defined from rational functions. This approach has been found to be computationally efficient. The impedance boundary condition is formulated under a differential form in order to improve the accuracy [12], and is used in the present eduction method for multimodal propagation.

The paper is organized as follows. Section 2 is devoted to the numerical modeling of the acoustic propagation under a grazing flow in a rectangular lined duct, and to the presentation of the broadband impedance boundary condition. The impedance eduction method itself is developed in Section 3 and validated in Section 4 first by comparison with experimental data from Jones et al. [2] for the case of plane wave propagation and then by comparison with a high fidelity numerical solution of the linearized Euler equations for the multimodal case. Concluding remarks are finally given in Section 5.

2. Acoustic propagation in the lined duct

2.1. Measurement setup

A rectangular duct including a treated section and the presence of a mean flow is chosen as the test channel for the impedance eduction. A sketch is shown in Fig. 1. The source and the exit planes of the computational domain are located at $x=0$ and $x = L_x$, respectively. The dimensions of the duct cross-section are $L_y \times L_z$. The lower and two-side walls are rigid. The upper wall is also rigid except of the lined region $L_1 < x < L_2$. To validate the impedance eduction method for plane wave propagation, the benchmark data of Jones et al. [2] is considered. The frequency range is $500 \leq f \leq 3000$ Hz and the dimensions of the channel are $L_x=0.812$ m, $L_1=0.203$ m, $L_2=0.609$ m and $L_y = L_z = 0.051$ m. A similar geometry is used to validate the multimodal test case, but with wider dimensions of the cross section, $L_y=0.15$ m and $L_z=0.3$ m, in order to observe a multimodal propagation for $f > 550$ Hz.

2.2. Linearized Euler equations

Sound propagation in a lined duct can be simulated by solving the Euler equations, linearized around a given mean flow of density ρ_0 and velocity $\mathbf{V_0}$. The mean pressure is assumed to be constant, the longitudinal pressure gradient to be small and the mean flow to be homentropic. The acoustic velocity $\mathbf{v}$ and the acoustic pressure p are obtained by solving the resulting system of equations written for an ideal gas, that is

$$\begin{cases} \dfrac{\partial p}{\partial t} + (\mathbf{V_0}\cdot\nabla)p + \rho_0 c_0^2 \nabla\cdot\mathbf{v} = \rho_0 c_0^2 Q \\ \dfrac{\partial \mathbf{v}}{\partial t} + (\mathbf{V_0}\cdot\nabla)\mathbf{v} + (\mathbf{v}\cdot\nabla)\mathbf{V_0} + \dfrac{1}{\rho_0}\nabla p = 0 \end{cases} \tag{1}$$

where c_0 is the speed of sound in air and Q is a possible source term, defined to generate an impulsive acoustic signal. These equations are discretized by low-dispersion and low-dissipation explicit numerical schemes, developed in computational aeroacoustics [16,17]. For the interior points, separated by at least five points from the boundary, the centered fourth-order finite-difference scheme of Bogey and Bailly [16] and the centered sixth order selective filter of Bogey et al. [18] are applied. For the boundary points in each direction, the eleven-point non-centered finite-difference schemes and selective filters of Berland et al. [17] are implemented. The optimized fourth-order six-stage Runge–Kutta algorithm proposed by Berland et al. [19] is used for time integration. The time-domain impedance boundary condition is presented in the next subsection. The inlet and outlet sections are assumed to be anechoic. Damping zones including the non-reflecting boundary conditions of Bogey and Bailly [20] are implemented. In NASA experiments, the termination is not perfectly anechoic. Its impedance could be included through an impedance condition at the outflow as proposed by Richter et al. [5] for instance. The deviation from a perfectly non-reflecting boundary condition, however, is expected to remain small here, as shown by comparison with

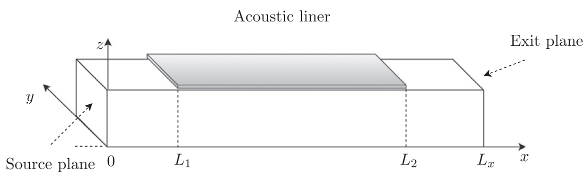

Fig. 1. Grazing flow impedance tube.

experimental data in Section 4.

2.3. Simulation parameters

The three-dimensional linearized Euler equations (1) are solved for the lined flow duct displayed in Fig. 1. The impulse source term is defined by

$$Q(\mathbf{x}, t) = \lambda(t)\exp\left[-\ln(2)\frac{(\mathbf{x} - \mathbf{x}_S)^2}{B^2}\right] \tag{2}$$

where the source signal $\lambda(t)$ is given by

$$\lambda(t) = \frac{t - t_s}{t_c}\exp\left[-\ln(2)\frac{(t - t_s)^2}{t_c^2}\right]H(t) \tag{3}$$

where H is the Heaviside function. The parameter t_s is a time shift, chosen so that $\lambda(t) = 0$ for $t < 0$, and t_c is a constant governing the frequency content of the source signal. They are set to $t_s = 8 \times 10^{-4}$ s and $t_c = 1.4 \times 10^{-4}$ s. The Gaussian half-width of the source is chosen to be $B = 8.3 \times 10^{-3}$ m and the source coordinates are $\mathbf{x_S} = (-0.05,\ 0.01,\ 0.008)$ m. Pressure and velocity in the frequency domain are obtained by Fourier transform of the time-domain solution. The mean velocity $\mathbf{V_0} = (V_{0\,x}, 0, 0)$ is prescribed using the following profile:

$$V_{0\,x}(y, z) = M\, c_0 \frac{n_y + 1}{n_y}\left(1 - \left|1 - \frac{2y}{L_y}\right|^{n_y}\right)\frac{n_z + 1}{n_z}\left(1 - \left|1 - \frac{2z}{L_z}\right|^{n_z}\right) \tag{4}$$

where $n_y = n_z = 12$ to recover a realistic mean shear flow. The Mach number $M = V_b/c_0$ is defined from the bulk velocity V_b. Measured data is acquired with 31 flush-mounted microphones on the wall opposite to the liner [2]. Three microphones are located upstream of the liner, three microphones are located downstream, and the other 25 microphones are situated in the lined section.

2.4. Broadband time-domain impedance boundary condition

The broadband impedance eduction method is developed in the time domain to avoid the tedious identification of the surface impedance for each frequency of interest. The surface impedance $Z(\omega)$ for a given angular frequency ω is primarily defined in the frequency domain by $\hat{p}(\omega) = Z(\omega)\hat{v}_n(\omega)$, with $\hat{v}_n = \hat{\mathbf{v}}\cdot\mathbf{n}$ where $\hat{p}(\omega)$ and $\hat{\mathbf{v}}(\omega)$ are the Fourier transforms of the acoustic pressure and acoustic velocity on the liner, respectively, and $\mathbf{n}$ is the normal unit vector pointing into the liner surface. Defining the time-domain surface impedance by

$$z(t) = \frac{1}{2\pi}\int_{-\infty}^{+\infty} Z(\omega)\mathrm{e}^{-\mathrm{i}\omega t}\mathrm{d}\omega \tag{5}$$

the frequency-domain impedance boundary condition is translated into the time domain via the convolution integral

$$p(t) = \int_{-\infty}^{t} v_n(t')z(t - t')\mathrm{d}t' \tag{6}$$

The analytical model must furthermore satisfy realizability conditions, in order to be physically admissible in the time domain. Following Rienstra [21], the impedance model must be causal, which means $z(t) = 0$ for $t < 0$. Furthermore, $z(t)$ must be real, so $Z(\omega)$ has to satisfy the reality condition $Z^*(\omega) = Z(-\omega)$. Finally, the condition $\mathrm{Re}[Z(\omega)] > 0$ has to be fulfilled for all $\omega \in \mathbb{R}$ since the impedance wall is passive. These conditions are not always verified by usual models defined in the Fourier space [21,22].

In the present study, the impedance model is chosen as a rational function of the form

$$Z(\omega) = \frac{a_0 + \cdots + a_N(-\mathrm{i}\omega)^N}{1 + \cdots + b_N(-\mathrm{i}\omega)^N} \tag{7}$$

where $(a_j)_{0\le j\le N}$ and $(b_j)_{1\le j\le N}$ are real coefficients. This formulation brings three advantages. First, a broadband impedance model is straightforwardly obtained. Second, the convolution integral can be evaluated at a small computational cost. Third, the coefficients can be easily chosen to guarantee the impedance to be physically admissible. By using a partial fraction decomposition, the rational function can be written as

$$Z(\omega) = Z_\infty + \sum_{k=1}^{P}\frac{A_k}{\lambda_k - \mathrm{i}\omega} + \sum_{k=1}^{S}\left(\frac{B_k + \mathrm{i}C_k}{\alpha_k + \mathrm{i}\beta_k - \mathrm{i}\omega} + \frac{B_k - \mathrm{i}C_k}{\alpha_k - \mathrm{i}\beta_k - \mathrm{i}\omega}\right) \tag{8}$$

where λ_k and $\alpha_k \pm \mathrm{i}\beta_k$ are, respectively, the real poles and complex conjugate pole pairs of $Z(\omega)$, P and S denote their number and Z_∞, A_k, B_k and C_k are numerical coefficients. Choosing $[Z_\infty,\ A_k,\ B_k,\ C_k] \in \mathbb{R}$ and $[\lambda_k,\ \alpha_k,\ \beta_k] \in \mathbb{R}^+$ ensures that the impedance model is causal and real. However, the passivity condition has to be checked for each set of coefficients. This type of impedance model is referred to as the multipole impedance model in the literature [23].

Other formulations of impedance models have been previously proposed for broadband eduction of liner impedance. In particular, two impedance models have been investigated by Richter et al. [5]. The first one is the so-called effective impedance (EFI) model

$$Z(\omega) = R_0 - \mathrm{i}\omega X_1 + \frac{X_{-1}}{-\mathrm{i}\omega} \tag{9}$$

and the second is the extended Helmholtz resonator (EHR) model

$$Z(\omega) = R_0 - \mathrm{i}\omega m + \beta \coth\left[\frac{1}{2}(-\mathrm{i}\omega T_l + \epsilon)\right] \tag{10}$$

where the coefficients of both models R_0, X_1, X_{-1}, m, β, T_l and ϵ have to be positive. Results obtained with these two models were compared to measurements performed for a ceramic tubular liner [2] and the EHR model was found to provide better results. [5] These authors have performed the broadband eduction using the EHR model, and the educed impedance is very close to that obtained in [2] with a single frequency eduction method. The EHR model was also used in [11,24] for broadband eduction of SDOF and DDOF liners. It is shown in Section 2.6 that the multipole impedance model can accurately describe the surface impedance of classical liners with only a few poles.

2.5. Implementation of a time-domain impedance boundary condition

The presence of a liner can also be described by a dual boundary condition expressed with the admittance $Y(\omega) = 1/Z(\omega)$. This formulation is more suitable to implement the liner boundary condition into the time domain for solving the linearized Euler equations (1) and is obtained by switching the velocity and the pressure in Eq. (6). The broadband admittance model is also approximated by a rational function similar to the impedance formulation (8)

$$Y(\omega) = Y_\infty + \sum_{k=1}^{\tilde{P}} \frac{\tilde{A}_k}{\tilde{\lambda}_k - \mathrm{i}\omega} + \sum_{k=1}^{\tilde{S}} \left(\frac{\tilde{B}_k + \mathrm{i}\tilde{C}_k}{\tilde{\alpha}_k + \mathrm{i}\tilde{\beta}_k - \mathrm{i}\omega} + \frac{\tilde{B}_k - \mathrm{i}\tilde{C}_k}{\tilde{\alpha}_k - \mathrm{i}\tilde{\beta}_k - \mathrm{i}\omega} \right) \tag{11}$$

The implementation of the boundary condition is nevertheless presented in terms of impedance below, to follow the more classical approach.

The direct computation of the convolution integral in the time domain is known to be computationally expensive in terms of memory space for typical applications [25]. Efforts have been thus undertaken to develop *ad hoc* numerical methods to reduce the computational cost. Tam and Auriault [14] have first proposed a formulation in the time domain applied to the EFI model (9). Related to previous works performed in electromagnetism, several methods have also been concerned with the multipole impedance model (8). Özyörük and Long [25] have introduced the Z-transform method, while Reymen et al. [12] have proposed the recursive convolution method, which has been extended by Li et al. [23] to include EFI model-like terms. Although it involves the reflection coefficient rather than the surface impedance, the impedance boundary condition proposed by Fung and Ju [26] can also be interpreted as a multipole impedance model formulation combined with a numerical recursive convolution method. Recursive convolution and Z-transform methods are very close, and permit to compute the convolution by simple algebraic recursive relations, which significantly reduces memory requirements. Some approximations on the time evolution of the acoustic quantities on the liner surface, by enforcing that the acoustic pressure or acoustic velocity is constant or varies linearly over each time step, are however made in these approaches. Dragna et al. [27] have shown that recursive convolution methods are at best second-order accurate in time. They limit the numerical accuracy when using high-order time-integration schemes, as generally done in aeroacoustics.

To overcome this drawback, a differential form for the multipole impedance model (8) has been developed by Joseph et al. [28], originally for applications in electromagnetism. The first step is to express the inverse Fourier transform of the impedance model $Z(\omega)$, which yields

$$z(t) = Z_\infty \delta(t) + \sum_{k=1}^{P} A_k \mathrm{e}^{-\lambda_k t} H(t) + \sum_{k=1}^{S} 2\left[B_k \cos(\beta_k t) + C_k \sin(\beta_k t)\right] \mathrm{e}^{-\alpha_k t} H(t) \tag{12}$$

where δ is the Dirac generalized function. By introducing this expression into the time-domain impedance boundary condition (6), the pressure can be expressed as

$$p(t) = Z_\infty v_n(t) + \sum_{k=1}^{P} A_k \phi_k(t) + \sum_{k=1}^{S} 2\left[B_k \psi_k^{(1)}(t) + C_k \psi_k^{(2)}(t)\right] \tag{13}$$

where the new terms ϕ_k and ψ_k, called accumulators in Reymen et al. [12], are given by

$$\phi_k(t) = \int_{-\infty}^{t} v_n(t')e^{-\lambda_k(t-t')}dt'$$
$$\psi_k^{(1)}(t) = \int_{-\infty}^{t} v_n(t')e^{-\alpha_k(t-t')}\cos(\beta_k(t-t'))dt'$$
$$\psi_k^{(2)}(t) = \int_{-\infty}^{t} v_n(t')e^{-\alpha_k(t-t')}\sin(\beta_k(t-t'))dt'$$

By differentiating with respect to time these relations, the first-order differential system governing the accumulators is then obtained:

$$\begin{cases} \dfrac{d\phi_k}{dt} + \lambda_k\phi_k(t) = v_n(t) \\ \dfrac{d\psi_k^{(1)}}{dt} + \alpha_k\psi_k^{(1)}(t) + \beta_k\psi_k^{(2)}(t) = v_n(t) \\ \dfrac{d\psi_k^{(2)}}{dt} + \alpha_k\psi_k^{(2)}(t) - \beta_k\psi_k^{(1)}(t) = 0 \end{cases} \tag{14}$$

This system is numerically integrated using the same time-marching scheme as for the LEE (1). Eqs. (14) along with Eq. (13) constitute the time-domain impedance boundary condition. This approach is referred to as the auxiliary differential equations (ADE) method. Contrary to recursive convolution or Z-transform methods, the accuracy of the numerical solution is not degraded while keeping low memory requirements. Indeed, the ADE method together with a low-storage Runge–Kutta algorithm for time-integration only demands two storages per accumulator.

A comparable approach has been developed by Bin et al. [29] to recast a broadband impedance to a differential form with application to the Ingard–Myers boundary condition. They used a multipole impedance model, written as a sum of stable second-order transfer functions. In their implementation, the constant term Z_∞ is not explicitly included and the accumulators are determined by a second-order differential system, which are the two main differences with respect to the present formulation. Finally, impedance boundary conditions for the multipole model have also been proposed in a differential form by Zhong et al. [30] from a state-space representation.

2.6. Specific broadband impedance models

A short review of some classical impedance models is now presented in order to demonstrate the ability of the multipole impedance model to interpolate accurately the function $Z(\omega)$. The multipole impedance approximation can be obtained from analytical models or measured impedance values using several algorithms. Among them, the vector fitting algorithm [31] already employed in [13] can be particularly mentioned. Only the minimum set of coefficients for impedance and corresponding admittance models is provided for each type of liner to cover the relevant frequency band with an error less than 5%. The results are summed up in Table 1.

2.6.1. Single Degree of Freedom (SDOF) liner

The SDOF liner consists in a facing sheet mounted on a honeycomb core with hardwall backing. Two types of coverings can be distinguished and provide a different response of the liner. The wire mesh panel gives a linear, insensitive to flow behavior, with a wide bandwidth. A liner with perforated sheet is non-linear, sensitive to flow, with a low bandwidth. The impedance can be modeled as follows:

$$\frac{Z}{\rho_0 c_0} = Z_{fs} + \coth(-ikd) \tag{15}$$

where Z_{fs} is the face sheet impedance, d is the core depth and $k = 2\pi f/c_0$ is the acoustic wavenumber. The impedance of a perforated SDOF liner using the set of parameters given in Table I of [24] is shown in Fig. 2. The face sheet impedance has been computed using the Guess model [32] for $M=0$. The impedance is approximated by Eq. (8) choosing five real poles, that is $P=5$ and $S=0$, for $f \in [200;\ 5000]$ Hz. The corresponding admittance (11) is modeled with $\tilde{P} = 3$ and $\tilde{S} = 1$ for the same frequency range.

2.6.2. Double Degree of Freedom (DDOF) liner

Double Degree of Freedom (DDOF) liners are composed of two layers of honeycomb cells divided by a porous septum, with different face sheets, backed by a rigid plate. Such liners are efficient over a wider frequency band with respect to SDOF liners. The liner impedance model is expressed as

$$\frac{Z}{\rho_0 c_0} = Z_{fs} + \frac{Z_s \cosh(-ikd_1)\sinh(-ikd_2) + \cosh(-ikd)}{Z_s \sinh(-ikd_1)\sinh(-ikd_2) + \sinh(-ikd)} \tag{16}$$

where Z_s is the septum impedance, d_2 is the septum backing cavity depth, d_1 is the face sheet backing space depth, and

Table 1
(a) Analytical modelling of various acoustic liners and number of poles required for their broadband (b) impedance and (c) admittance approximation, see Eq. (8).

Liner	Sketch	(a) Impedance model	(b) Broadband impedance model	(c) Broadband admittance model
Single degree of freedom (SDOF) [38,24]	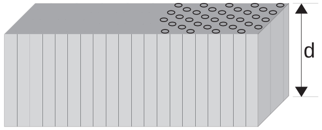	$\frac{Z}{\rho_0 c_0} = Z_{fs} + \coth(-ikd)$	$f \in [200;\ 5000]$ Hz $P=5;\ S=0;$	$\tilde{P}=3;\ \tilde{S}=1;$
Double Degree of Freedom (DDOF) [33,24]	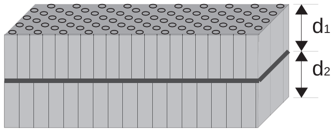	$\frac{Z}{\rho_0 c_0} = Z_{fs} + \frac{Z_s \cosh(-ikd_1)\sinh(-ikd_2) + \cosh(-ikd)}{Z_s \sinh(-ikd_1)\sinh(-ikd_2) + \sinh(-ikd)}$	$f \in [200;\ 5000]$ Hz $P=4;\ S=1;$	$\tilde{P}=1;\ \tilde{S}=2;$
Bulk absorber liner [34]	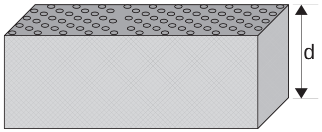	$\frac{Z}{\rho_0 c_0} = Z_{fs} + Z_c \coth(-ik_c d)$	$f \in [500;\ 5000]$ Hz $P=1;\ S=1;$	$\tilde{P}=0;\ \tilde{S}=2$
Hybrid active–passive liner [35]	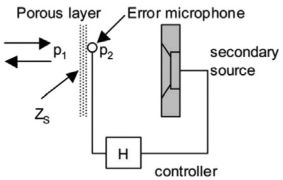	active mode: $\frac{Z}{\rho_0 c_0} = Z_{fs}$ passive mode: $\frac{Z}{\rho_0 c_0} = Z_{fs} + \coth(-ikd)$	$f \in [200;\ 3000]$ Hz $P=1;\ S=1;$	$\tilde{P}=0;\ \tilde{S}=1;$
Ceramic tubular liner [2]	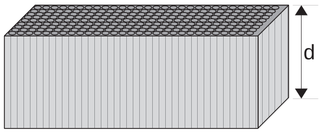	$\frac{Z}{\rho_0 c_0} = \frac{1}{\sigma} \coth(-ik_{\mathrm{tube}} d)$	$f \in [500;\ 3000]$ Hz $P=1;\ S=1;$	$\tilde{P}=0;\ \tilde{S}=2;$

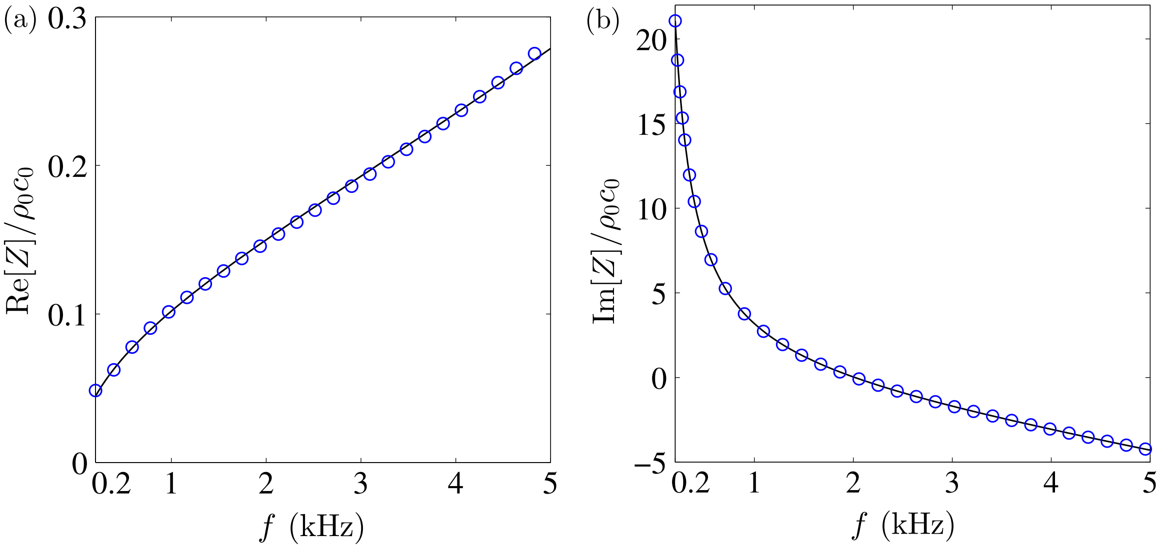

Fig. 2. Real (a) and imaginary (b) parts (circle symbols) of impedance for the SDOF liner (15), and comparison with their approximations by the multipole impedance model (8) in solid line.

$d = d_1 + d_2$. The impedance $Z(\omega)$ can be approximated using four real poles and one pair of complex conjugate poles, $P=4$ and $S=1$, and the admittance by $\tilde{P} = 1$ and $\tilde{S} = 2$ for $f \in [200;\ 5000]$ Hz. The impedance of a DDOF liner, with perforated face sheet and septum parameters given by Burd in [33] for a conventional liner is presented in Fig. 3. The face sheet and septum impedances have been computed with the Guess model [32] for $M=0$.

2.6.3. Bulk absorber liner

In a bulk absorber liner the honeycomb structure is replaced by a porous bulk material. The surface impedance of the liner is given by

$$\frac{Z}{\rho_0 c_0} = Z_{fs} + Z_c \coth(-\mathrm{i}k_c d) \tag{17}$$

where Z_c is the characteristic impedance and k_c is the acoustic wavenumber inside the porous material. An example of surface impedance of a bulk liner, with the parameters given in [34], is shown in Fig. 4. For the multipole impedance model (8) one real pole and one pair of complex conjugate poles, $P=1$ and $S=1$, are needed for $f \in [200;\ 5000]$ Hz. The

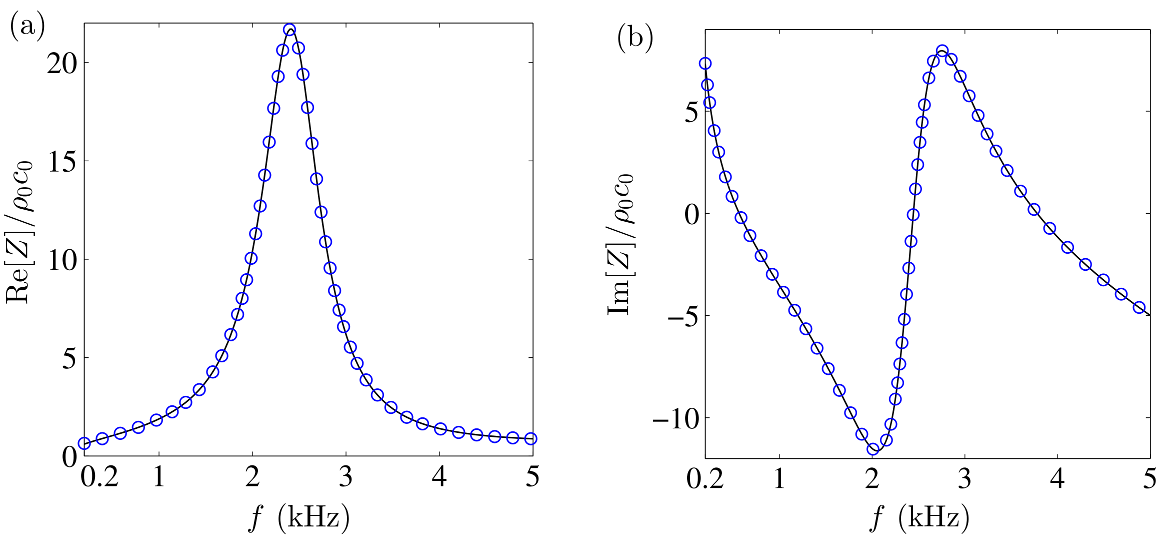

Fig. 3. Real (a) and imaginary (b) parts of impedance (circle symbols) for the DDOF liner (16) and comparison with their approximations by the multipole impedance model (8) in solid line.

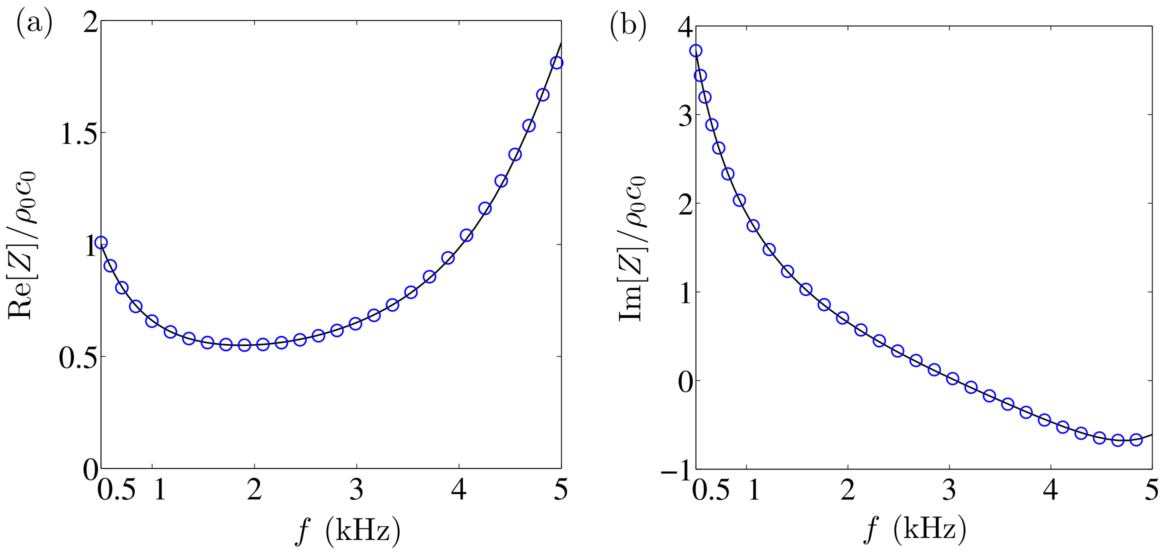

Fig. 4. Real (a) and imaginary (b) parts of a bulk liner impedance (circle symbols), see Eq. (17), and comparison with their approximations by the multipole impedance model (8) in solid line. Characteristics of the liner can be found in [34].

corresponding admittance is approximated with $\tilde{P} = 1$ and $\tilde{S} = 2$.

2.6.4. Hybrid active–passive liner

Hybrid active–passive liner has been developed for broadband noise reduction in flow ducts. Passive absorbent properties of a porous layer are combined with active control cells behind the resistive screen, as described by Betgen et al. [35]. At high frequencies, active control sources are turned off and the hybrid liner acts as a classical SDOF resonator modeled by Eq. (15). At lower frequencies, active noise control is switched on with the aim of adapting the surface impedance of the liner. A good performance over a broad frequency range is then obtained. The resulting surface impedance can be expressed as

$$\begin{cases} \dfrac{Z}{\rho_0 c_0} = Z_{fs} \text{ in active mode} \\ \dfrac{Z}{\rho_0 c_0} = Z_{fs} + \coth(-\mathrm{i}kd) \text{ in passive mode} \end{cases} \tag{18}$$

where Z_{fs} is the resistive screen impedance and d is the distance between the resistive screen and the cells. The impedance $Z(\omega)$ can again be approximated using $P=1$ and $S=1$ and the corresponding admittance with $\tilde{P} = 0$ and $\tilde{S} = 1$ for $f \in [200;\ 3000]$ Hz.

2.6.5. Ceramic tubular liner

The last considered example is the ceramic tubular liner that is often used in academic studies, as its impedance is not sensitive to the presence of a flow. It consists of a densely packed narrow ceramic tubes embedded in a ceramic matrix. The tubes of depth d are rigidly terminated such that each is isolated from its neighbor to ensure a locally reacting structure. The channel diameter is small enough to ensure that grazing flow effects are insignificant with respect to internal viscous losses [2]. The impedance can be modeled as

$$\frac{Z}{\rho_0 c_0} = \frac{1}{\sigma} \coth(-\mathrm{i}k_{\mathrm{tube}} d) \tag{19}$$

where σ is the porosity of the surface of the material, and k_{tube} is the acoustic wavenumber inside the tubes [36,37]. The resistance and the reactance are neither constant nor linearly behaving on the typical frequency range of interest. For both cases, the impedance $Z(\omega)$ can be approximated using one real pole and one pair of complex conjugate poles, *i.e.* $P=1$ and $S=1$ for $f \in [500;\ 3000]$ Hz. The corresponding admittance formulation is obtained with $\tilde{P} = 0$ and $\tilde{S} = 2$.

3. Impedance eduction method

The acoustic impedance is determined by minimizing an error function between the calculated and the measured sound field inside the channel. Most of the existing eduction methods are usually applied in the frequency range below the duct

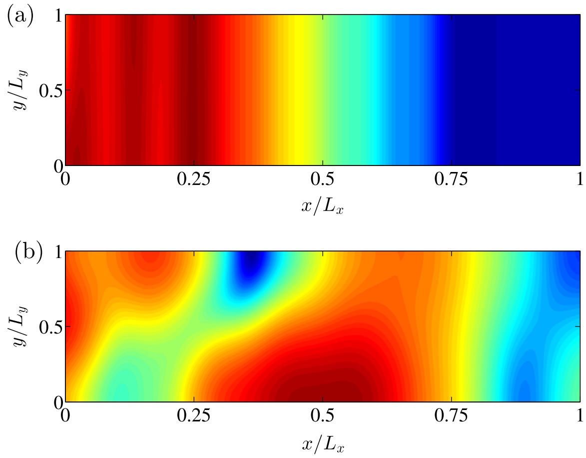

Fig. 5. Sound pressure level (dB) on the wall opposite to the liner at $z = L_z$, with f=2000 Hz, M=0 and $Z = 4.18 + 0.77i$; (a) small cross-section duct (scale from 92 to 100 dB) and (b) large cross-section duct (scale range from 61 to 79 dB).

cutoff frequency, allowing only plane waves to propagate. In this study a methodology is developed for multimodal acoustic propagation. One of the main issues with multimodal propagation is that the spatial distribution of the sound field is no longer well-structured by comparison with plane waves. As an example, the sound pressure level (SPL) at the wall opposite the liner for a frequency f=2000 Hz is shown in Fig. 5 for the two rectangular ducts described in Section 2.1. The LEE are forced with the monopolar source described in Section 2.3. In the small duct, the only propagating mode is the plane wave mode. As expected, the sound pressure level pattern is that of a plane wave propagating inside a lined duct. The SPL is almost constant in the solid wall regions $x/L_x < 0.25$ and $x/L_x > 0.75$, but decreases with the axial distance in the treated region. For the large duct, the first seven modes are cut-on. The acoustic field is far more complex, and large variations of the SPL can now be observed along the y-direction.

Multimodal propagation demands a larger number of microphones to describe the pressure and velocity fields, which leads to a significant additional cost. To overcome this difficulty, the duct insertion loss is introduced as a global energetic indicator

$$\mathrm{IL} = 10\,\log_{10}(W_R/W_L) \tag{20}$$

where W_R is the transmitted sound power computed at the exit plane of the hard-wall duct, see Fig. 1 and W_L is the transmitted sound power computed at the exit plane of the lined duct. The power W is obtained by integration of the sound intensity I over the cross-section of the duct

$$W(x) = \iint I(x,y,z)\mathrm{d}y\mathrm{d}z \tag{21}$$

where

$$I(x,y,z) = \frac{1}{2}\left[(1+M^2)\,\mathrm{Re}(\hat{p}\;\hat{v}_x^*) + \frac{M}{\rho_0 c_0}\;\mathrm{Re}(\hat{p}\;\hat{p}^*) + M\rho_0 c_0\;\mathrm{Re}(\hat{v}_x\;\hat{v}_x^*)\right] \tag{22}$$

is a good approximation of the acoustic intensity in the presence of a flow [39]. Therefore, the corresponding objective function f_1 can be formulated as follows:

$$f_1[Z(\mathbf{X})] = \sum_{i=1}^{N_{\mathrm{IL}}} \left(\mathrm{IL}_{\mathrm{measured}} - \mathrm{IL}_{\mathrm{FDTD}}\right)^2 \tag{23}$$

where $\mathbf{X} = [Z_\infty,\ A_k,\ B_k,\ C_k,\ \lambda_k,\ \alpha_k,\ \beta_k]$ are the coefficients of the multipole impedance model, $\mathrm{IL}_{\mathrm{measured}}$ and $\mathrm{IL}_{\mathrm{FDTD}}$ are the vectors of the insertion loss for the N_{IL} considered frequencies, obtained from measurements and from simulations of the linearized Euler equations.

The eduction method based on the sole objective function in Eq. (23) relies on a global energetic variable. An additional local quantity can be introduced in order to improve the robustness of the method. The acoustic pressure along the duct wall opposite to the liner for frequencies below the rig cutoff frequency is a good candidate. Indeed, it is an easily measurable quantity and is directly related to the liner impedance. A second objective function f_2 is therefore proposed:

$$f_2[Z(\mathbf{X})] = \sum_{i=1}^{N_P} \sum_{l=1}^{N_M} \left\| \hat{p}^{\,i}_{l\ \mathrm{measured}} - \hat{p}^{\,i}_{l\ \mathrm{FDTD}} \right\|^2 \tag{24}$$

where $\hat{p}_{l\,\text{measured}}^{\,i}$ and $\hat{p}_{l\,\text{FDTD}}^{\,i}$ are the complex pressure values obtained from the measurements and from the numerical simulations, for the microphone positions $l \in [1;\ N_M]$ and for the i-th frequency. The number N_P of considered frequencies below the duct cutoff frequency depends on the measurement facility. As an illustration, for the large cross-section duct used for the validation of multimodal sound propagation, the cutoff frequency is $f=550$ Hz for $M=0$. Finally, the optimization problem to solve can be written as the following statement:

$$\begin{aligned} &\min && f_1[Z(\mathbf{X})] = \sum_{i=1}^{N_{\text{IL}}} \left(\text{IL}_{\text{measured}} - \text{IL}_{\text{FDTD}}\right)^2 \\ &\min && f_2[Z(\mathbf{X})] = \sum_{i=1}^{N_P} \sum_{l=1}^{N_M} \left\| \hat{p}_{l\,\text{measured}}^{\,i} - \hat{p}_{l\,\text{FDTD}}^{\,i} \right\|^2 \\ &\text{such that} && \underline{x}_j \le x_j \le \overline{x_j}, \quad \mathbf{X} = \{x_j\} \in \mathbb{R}^m \\ & && \text{Re}[Z(\mathbf{X})] > 0 \end{aligned} \tag{25}$$

with $j = 1, .., m$, and where m is number of the impedance model coefficients to be identified. The variables x_j are usually restricted by side constraints $\underline{x_j}$ and $\overline{x_j}$, which are lower and upper limits that reflect the multipole model definition domain.

The set of the coefficients of the broadband impedance model that minimize the objective functions f_1 and f_2 must be identified. In order to deal with this multiobjective optimization problem, two major categories are used in engineering, namely with *a priori* articulation of preferences and with *a posteriori* articulation of preferences. A comprehensive review can be found in Marler and Arora [40]. For *a priori* methods, the relative importance of the objective functions has to be defined before running the optimization algorithm. These functions are weighted thanks to a relative preference factor known in advance, which is not always possible. The so-called *a posteriori* methods provide multiple trade-off solutions with a wide range of values for the objectives, and the retained solution has to be chosen using higher-level information. Genetic algorithms are often preferred. They do not require gradient calculation, and can be effective regardless of the nature of the objective functions and constraints. Here the evolutionary genetic algorithm Non-dominated Sorting Genetic Algorithm-II (NSGA-II) presented in Deb et al. [41] is employed. A set of Pareto optimal solutions is then produced, and the solution which optimizes all the objectives simultaneously is finally selected. When this solution [42] cannot be found, preferences on the objective functions values are imposed. The minimization of the insertion loss IL through the objective function f_1 is here preferred. The convergence of the present impedance eduction method is obtained thanks to the three following choices: first a global energetic variable, such as the insertion loss, second a local quantity, here the fluctuating pressure provided by a few microphones for a frequency range where only plane waves propagate, and third the broadband feature of the eduction process involving a prescribed shape of the impedance for the whole studied frequency range.

4. Validation of the method

All the results presented in this study have been obtained by considering a ceramic tubular liner modeled by the multipole admittance model (11) with $\tilde{P} = 0$ and $\tilde{S} = 2$. The eduction method is aimed at determining the 9 coefficients $[\tilde{Y}_\infty,\ \tilde{B}_k,\ \tilde{C}_k,\ \tilde{\alpha}_k,\ \tilde{\beta}_k]$ for $k=1, 2$.

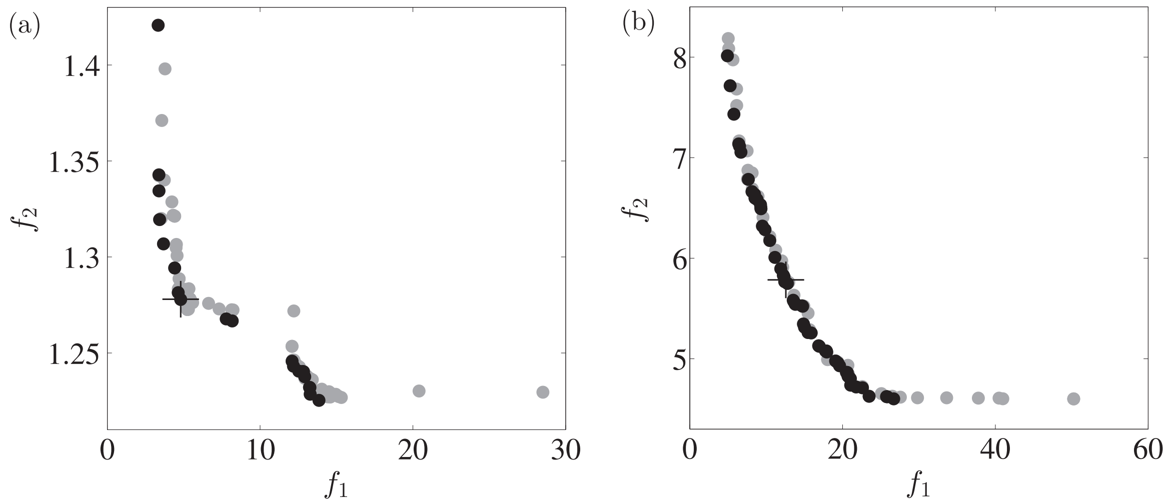

Fig. 6. Solutions provided by the NSGA-II algorithm: (a) $M=0$, (b) $M=0.335$. All solutions are marked with gray dots ●, non-dominated solutions with black dots ● and the chosen optimal solution is marked with a cross +.

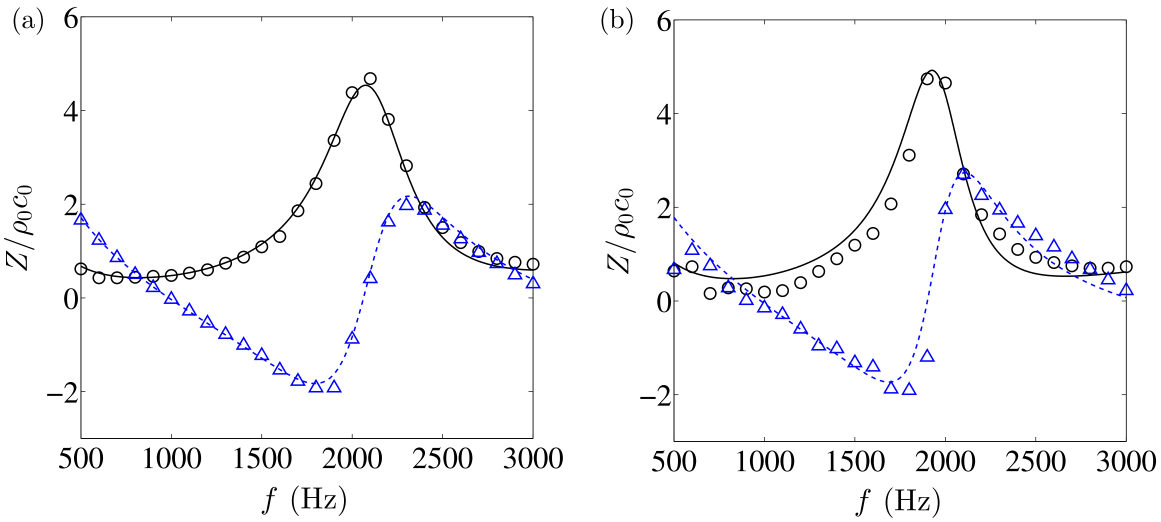

Fig. 7. Real (solid line) and imaginary (dashed line) parts of the educed impedance obtained using the LEEs solver, as a function of the frequency. Corresponding real and imaginary parts of the NASA educed impedance [2] are marked by circles and triangles, respectively. (a) $M=0$ and (b) $M=0.335$.

4.1. Validation for plane wave propagation

The proposed eduction method is first validated by the benchmark data provided by Jones et al. [2]. The pressure field was measured at 31 locations on the wall opposite to the liner for frequencies below the cut-off frequency of the duct and the liner admittance was educed. For plane waves, the insertion loss IL is given by

$$\mathrm{IL} = 10\log_{10}\left(\frac{\| \hat{p}_I \|^2}{\| \hat{p}_T \|^2}\right) \tag{26}$$

where $\hat{p}_I$ and $\hat{p}_T$ are the incident and transmitted pressure, respectively. The IL values can be directly computed from the benchmark data [2]. The present method has been applied for four values of the Mach number $M=0$, 0.079, 0.255 and 0.335. The case at $M=0.4$ has also been investigated. In this case, a vortical instability wave for $f=1000$ Hz develops from the point $x = L_1$. This instability wave is also observed in experiments [2], and in some numerical studies, *e.g.* Burak et al. [43]. It must be recognized, however, that the separation between spurious and physical waves is quite tricky, as recently examined in detail by Gabard and Brambley [44]. This discussion is however out of the scope of the present study. The insertion loss is determined for $N_{\mathrm{IL}} = 26$ frequencies from 500 Hz to 3000 Hz. For the second objective function, five frequencies are considered from 500 Hz to 900 Hz. NSGA optimization is carried out with 50 elements in 30 populations. These values have been chosen according to Vrajitoru [45], who have shown that larger populations have more chances to improve the effectiveness with limited time resources. The computational area is discretized by $500 \times 26 \times 26$ points with a uniform spatial step $\Delta x = \Delta y = \Delta z = 4.17 \times 10^{-3}$ m. The simulation is run up to $t_{max} = 0.03$ s with the step of $\Delta t = 1 \times 10^{-5}$ s. The computational time is about 10 min on a desktop computer for a single simulation that gives around 10 days for the whole optimization loop using a single core computer. Genetic algorithm is however well suited to parallel computing. As an illustration, the time is reduced to two days using 6 cores.

The last population of the optimization process performed by the NSGA-II algorithm for $M=0$ and $M=0.335$ is shown in Fig. 6. Among all these results, the important data are the non-dominated solutions representing a compromise between the two objective functions. These solutions represented by black dots in Fig. 6 form the Pareto front. Both Pareto fronts are almost vertical regarding the objective function f_2, meaning that for a minimum of the objective function f_1, the minimum of f_2 can be selected. The solution that optimizes both objectives simultaneously is chosen, and the corresponding identified impedance is plotted in Fig. 7 for $M=0$ and $M=0.335$. The educed impedance is found in close agreement with that determined by NASA over the whole frequency band of interest, with or without the presence of a flow. Similar results are

Table 2
Coefficients of the broadband admittance impedance model (11) normalized by $\rho_0 c_0$, educed for the case of plane waves propagation. Coefficients $\tilde{\alpha}_i$ and $\tilde{\beta}_i$ are in s^{-1}.

Mach	$\tilde{Y}_\infty$	$\tilde{B}_1$	$\tilde{B}_2$	$\tilde{C}_1$	$\tilde{C}_2$	$\tilde{\alpha}_1$	$\tilde{\alpha}_2$	$\tilde{\beta}_1$	$\tilde{\beta}_2$
$M=0$	0.2576	2953	1993	−1634	−415.6	2348	1000	19,674	6004
$M=0.335$	0.3915	2207	1767	−2243	−417.3	2169	1001	17,826	5942

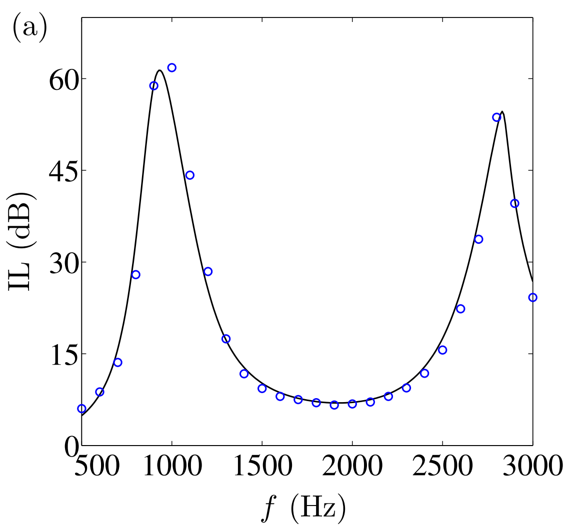

Fig. 8. Insertion loss values computed for the educed impedance using the LEEs solver (solid line) and determined from NASA measurements (circles), as a function of the frequency. (a) $M=0$ and (b) $M=0.335$.

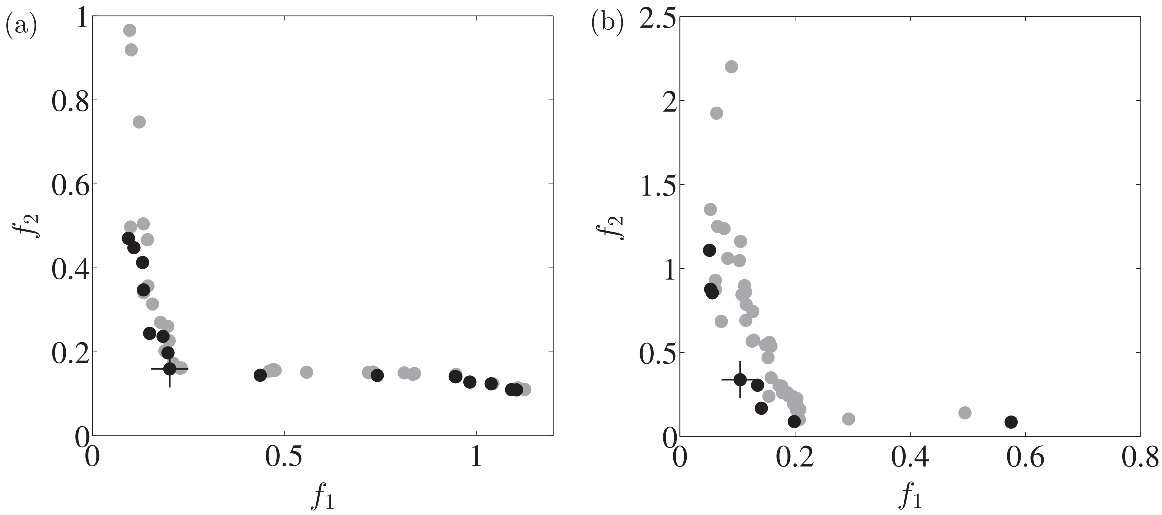

Fig. 9. Solutions provided by the NSGA-II algorithm: (a) $M=0$, (b) $M=0.4$. All solutions are marked with gray dots ●, non-dominated solutions with black dots ● and optimal solution is marked with a cross +.

obtained for the other cases with $M=0.079$ and 0.255. The small discrepancies between the educed impedances for $M=0.335$ could be attributed to the difference in the termination boundary condition. In the NASA eduction procedure [2], the exit impedance was taken into account, whereas in this study the termination is assumed to be anechoic. The coefficients of the admittance (11) are provided in Table 2. The comparison between the insertion loss IL determined from NASA pressure measurements, and obtained by solving the LEE system for the educed liner impedance are plotted in Fig. 8. A close agreement is obtained for $M=0$. For the case $M=0.335$, discrepancies are observed near resonances, for $f=1100$ Hz and $f>2800$ Hz. The IL values computed from the educed impedance underestimate those determined from NASA data.

4.2. Validation for multimodal wave propagation

No measurement is currently available in the framework of this study. The data used to assess the eduction process have thus been numerically synthesized by solving the LEE system (1). Two Mach numbers are considered $M=0$ and $M=0.4$. For the latter case, the vortical instability wave exhibited for the small cross-section duct has not been observed. The values of the ceramic tubular liner admittance presented in [2] are interpolated by the multipole admittance model (8). A set of coefficients is computed for each considered Mach number, using the vector fitting algorithm [31]. For the case $M=0$, the

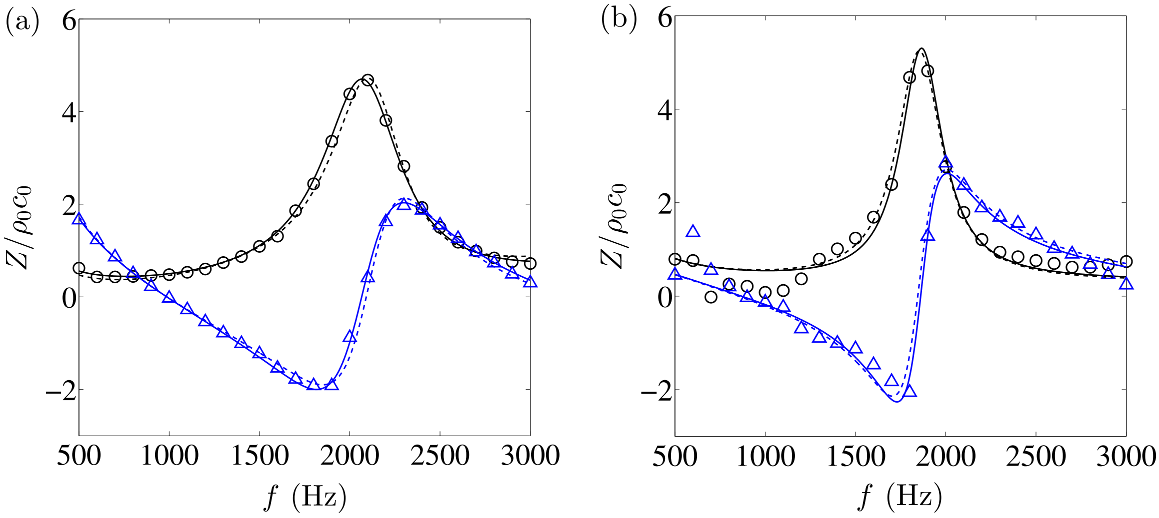

Fig. 10. Real and imaginary parts of the impedance as a function of the frequency. The real and imaginary parts of the reference NASA educed impedance [2] are marked by circles and triangles, respectively. Solid lines correspond to the NASA educed impedance fitted by the multipole model, the educed impedance is plotted in dashlines. (a) $M=0$ and (b) $M=0.4$.

Table 3
Coefficients of the broadband admittance impedance model (11) normalized by $\rho_0 c_0$, educed for the case of multimodal propagation. Coefficients $\tilde{\alpha}_i$ and $\tilde{\beta}_i$ are in s^{-1}.

Mach	$\tilde{Y}_\infty$	$\tilde{B}_1$	$\tilde{B}_2$	$\tilde{C}_1$	$\tilde{C}_2$	$\tilde{\alpha}_1$	$\tilde{\alpha}_2$	$\tilde{\beta}_1$	$\tilde{\beta}_2$
$M=0$	0.3679	1698	2075	−2283	−620.5	3014	1002	18,258	5940
$M=0.4$	0.2816	24,865	3916	−15,222	705.8	9433	2259	28,387	5721

large cross-section channel is discretized by a grid of $500 \times 21 \times 43$ points. For the case $M=0.4$, the grid contains $500 \times 37 \times 71$ points to correctly take into account the presence of the mean flow (4). As in the NASA experimental study, the fluctuating pressure is recorded at the 31 microphones located on the wall opposite to the liner. The simulation is performed up to $t_{\max} = 0.03$ s with a step of $\Delta t = 1 \times 10^{-5}$ s. The transmitted sound power W_L is also calculated. The same process is repeated for the hard-wall configuration with $t_{\max} = 0.1$ s in order to determine W_R, and to finally compute the insertion loss (20). More details regarding this tricky issue are provided in Appendix.

The impedance eduction is then performed using the previous synthesized data. The first objective function f_1 is calculated with $N_{IL} = 26$ frequencies from 500 Hz to 3000 Hz. Six frequencies below the no-flow cutoff frequency of the duct are considered for the second objective function f_2, from 500 Hz to 550 Hz. The parameters for NSGA optimization are the same as for the case of plane waves. The computational time is about 20 min for a given configuration, and approximately 20 days for the whole optimization loop using a single core computer, and around 4 days using parallel computing on six cores. The last population resulting from the genetic algorithm is displayed in Fig. 9. The objective functions that form the Pareto fronts reach smaller values than those found in the previous case for plane wave propagation, see Fig. 6. No experimental spurious noise is indeed present in this second case, involving only data provided by numerical simulations. The selected optimal solution is indicated by a cross, and the corresponding impedance is shown in Fig. 10 for both Mach numbers. A good agreement is found with the initial data used in the high-fidelity simulation to generate the numerical experiment. Similar results are obtained for both Mach numbers, and over the whole frequency band of interest. For completeness, the coefficients of the educed admittance are provided in Table 3.

5. Conclusion

A new broadband impedance eduction method has been developed in this work. The method offers the possibility to educe the impedance of liners under a grazing flow and for multimodal sound propagation. Since a broadband formulation of the impedance boundary condition is implemented, the eduction process is conducted in the time domain for all the considered frequency simultaneously.

The liner impedance is sought as a rational function of the frequency. The number of real poles and complex conjugate pole pairs is chosen depending on the liner type and the frequency band of interest. The coefficients of the impedance approximation are obtained through the resolution of a multi-objective problem. The two objectives are to minimize the error between measured and simulated values of a global energetic variable, namely the insertion loss, and of a local quantity, which is the fluctuating pressure at frequencies below the rig cut-off frequency. The genetic algorithm NSGA-II is used to solve this multi-objective optimization problem, whatever the form of the broadband impedance model is. Various liners can thus be studied with the same optimization code.

The present method is validated for plane wave propagation by using the benchmark data provided by Jones et al. [2]. The validation of the multimodal propagation is conducted using synthesized numerical data. The next step will be to consider experimental data for the multimodal propagation and several types of conventional liners. The study of the algorithm convergence as well as its stability toward the model parameters will be conducted. This can help the users to reduce the number of design variables and to identify which model parameters affect the solution.

Acknowledgments

This work was performed within the framework of the Labex CeLyA of Université de Lyon, the program Investissements d'Avenir (ANR-10-LABX-0060/ ANR-11-IDEX-0007) operated by the French National Research Agency (ANR) and was carried out in collaboration with Aircelle (technical monitor Marc Versaevel). The authors would like to acknowledge the financial support from the European Union Seventh Framework Programme (FP7) through the ENOVAL project under grant agreement number 604999. In addition, the authors would like to thank Dr. Michael Jones (NASA) for providing the benchmark data used for the validation.

Appendix: Insertion loss computation for multimodal acoustic propagation

This appendix aims to provide details about the choice of parameters for the numerical solutions and the computation of the sound power. The time-series of the acoustic pressure at the center of the exit plane are represented in Fig. 11 using the impulsive Gaussian source (2) and with $M=0$. For a rigid duct in Fig. 11(a), the signal is composed of a direct arrival, which propagates along a straight line from the source to the observer, and of a large number of arrivals, corresponding to reflected waves on the duct walls. The acoustic energy remains trapped in the duct and the sound pressure slowly decays with time. For instance, the amplitude of the pressure at $t=0.06$ s, corresponding to a propagation distance of about 25 times the duct length, is equal to the third of the direct arrival amplitude. An accurate evaluation of the sound intensity therefore requires a sufficiently long simulation time, so that most of the energy of the impulsive acoustic signal is captured at the exit plane. The corresponding time-series for a lined duct is shown in Fig. 11(b). The pressure decreases much more quickly with time, and the signal energy can be neglected for $t > 0.02$ s.

For comparison, the time-series of the acoustic pressure are represented in Fig. 12 for an impulsive source forcing plane waves only, defined by

$$Q(\mathbf{x}, t) = \lambda(t)\exp\left(-\ln(2)\frac{x^2}{B^2}\right)$$

with the same numerical parameters than for the monopolar source (2). For the case of a rigid duct in Fig. 12(a), a single arrival phase is observed. As expected, the plane wave generated by the source propagates in the duct without being

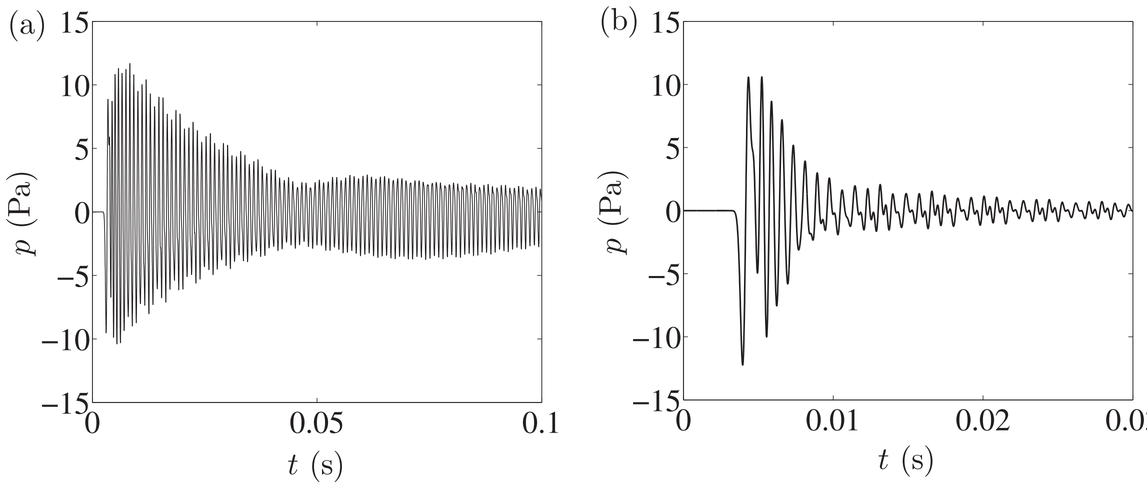

Fig. 11. Time series of the acoustic pressure p at the center of the exit plane: (a) for a rigid duct and (b) for a lined duct. The Mach number is $M=0$.

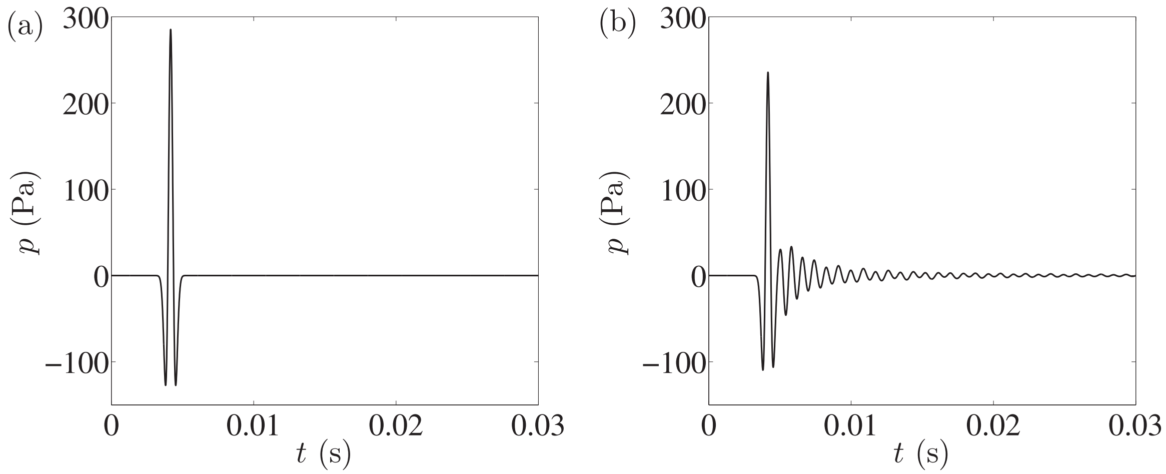

Fig. 12. Time series of the acoustic pressure p at the center of the exit plane: (a) for a rigid duct and (b) for a lined duct. The Mach number is $M = 0$.

attenuated or reflected at the duct wall. The simulation time for plane wave propagation can be dramatically reduced compared to that for multimodal propagation. The signal obtained for a lined duct is shown in Fig. 12(b). The first contribution is related to the plane wave generated by the source and is slightly attenuated compared to the rigid duct case due to the liner. Small amplitude oscillations are observed at the tail of the signal. They are associated with acoustic diffraction at the liner edges.

As indicated above, the evaluation of the transmitted sound power for multimodal propagation can be significantly affected by an inappropriate simulation time. In order to carefully choose this parameter in the eduction process, a convergence study has been carried out. The transmitted sound power has been computed for three simulation times $t_{max} = 0.08$, 0.09 and 0.1 s, and is shown as a function of the frequency in Fig. 13. As already noted by Gabard [46], large peaks are observed for the transmitted sound power spectrum at the duct cutoff frequencies for the rigid duct, see Fig. 13(a). Because the source (2) is located close to the center of the cross-section, the symmetrical modes with cutoff frequencies of 1140, 2280 and 2550 Hz are preferentially excited. Moreover, the sound power spectra for a simulation time of 0.09 s and 0.1 s are almost superimposed. A simulation time $t_{max} = 0.1$ s appears to be long enough in the case of a rigid duct. Choosing the smaller simulation time of 0.08 s leads to an error on the peak amplitudes whereas the broadband component of the spectrum remains accurately predicted. Smaller peaks are also observed in Fig. 13(b) for the case of a lined duct, and no significant difference is observed for the three simulation times. In this case, $t_{max} = 0.03$ s is a long enough simulation time to estimate the transmitted sound power. Finally, acoustic levels are averaged over a 100 Hz frequency band in practice to overcome this difficulty.

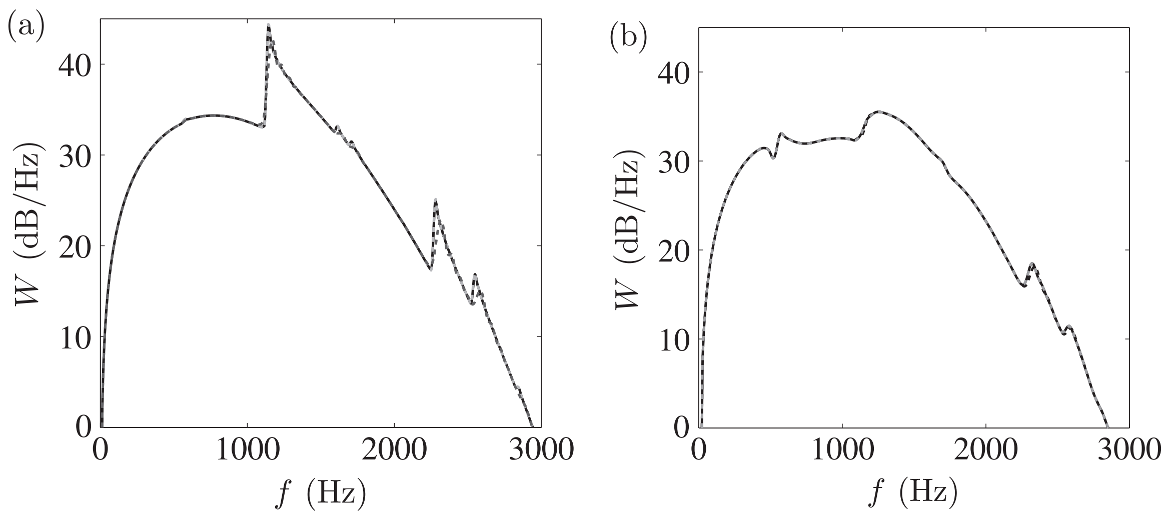

Fig. 13. Transmitted sound power W calculated for the large cross-section duct with the impulse multimodal source. (a) W_R, rigid duct, dashed black line for $t_{max} = 0.08$ s, dashed gray line for $t_{max} = 0.09$ s, solid black line for $t_{max} = 0.1$ s. (b) W_L, lined duct, dashed black line for $t_{max} = 0.02$ s, dashed gray line for $t_{max} = 0.028$ s, and solid black line for $t_{max} = 0.03$ s.

References

[1] W.R. Watson, M.G. Jones, S.E. Tanner, T.L. Parrott, Validation of a numerical method for extracting liner impedance, *AIAA J.* 34 (3) (1996) 548–554.
[2] M.G. Jones, W.R. Watson, T.L. Parrott, Benchmark data for evaluation of aeroacoustic propagation codes with grazing flow, in: 11th AIAA/CEAS Aeroacoustics Conference, 23–25 May, Monterey, CA, USA, AIAA Paper 2005-2853, 2005, pp. 1–18.
[3] T. Elnady, H. Bodén, B. Elhadidi, Validation of an inverse semi-analytical technique to educe liner impedance, *AIAA J.* 47 (12) (2009) 2836–2844.
[4] N. Sellen, M. Cuesta, M.-A. Galland, Noise reduction in a flow duct: *implementation of a hybrid passive/active solution*, *J. Sound Vib.* 297 (3) (2006) 492–511.
[5] C. Richter, F.H. Thiele, X. Li, M. Zhuang, Comparison of time-domain impedance boundary conditions for lined duct flows, *AIAA J.* 45 (6) (2007) 1933–1945.
[6] W. Eversman, J.M. Gallman, Impedance eduction with an extended search procedure, *AIAA J.* 49 (9) (2011) 1960–1970.
[7] E. Piot, F. Simon, J. Primus, Liner impedance eduction technique based on velocity fields, in: 18th AIAA/CEAS Aeroacoustics Conference, 4–6 June, Colorado Springs, CO, USA, AIAA Paper 2012-2198, 2012, pp. 1–18.
[8] J. Primus, E. Piot, F. Simon, An adjoint-based method for liner impedance eduction: *validation and numerical investigation*, *J. Sound Vib.* 332 (1) (2013) 58–75.
[9] W.R. Watson, C.H. Gerhold, M.G. Jones, J.C. June, Single mode theory for impedance eduction in large-scale ducts with grazing flow, in: 20th AIAA/CEAS Aeroacoustics Conference, 16–20 June, Atlanta, GA, USA, AIAA Paper 2014-3351, 2014, pp. 1–15.
[10] Y. Buot de l'Épine, J.-D. Chazot, J.-M. Ville, Bayesian identification of acoustic impedance in treated ducts, *J. Acoust. Soc. Am.* 138 (1) (2015) EL114–EL119.
[11] C. Richter, J.A. Hay, N. Schönwald, S. Busse, F. Thiele, et al., A review of time-domain impedance modelling and applications, *J. Sound Vib.* 330 (16) (2011) 3859–3873.
[12] Y. Reymen, M. Baelmans, W. Desmet, Efficient implementation of Tam and Auriault's time-domain impedance boundary condition, *AIAA J.* 46 (9) (2008) 2368–2376.
[13] Y. Reymen, M. Baelmans, W. Desmet, Time-domain impedance formulation suited for broadband simulations, in: 13th AIAA/CEAS Aeroacoustics Conference, 21–23 May, Rome, Italy, AIAA Paper 2007-3519, 2007, pp. 1–11.
[14] C.K. Tam, L. Auriault, Time-domain impedance boundary conditions for computational aeroacoustics, *AIAA J.* 34 (5) (1996) 917–923.
[15] B. Cotté, P. Blanc-Benon, C. Bogey, F. Poisson, Time-domain impedance boundary conditions for simulations of outdoor sound propagation, *AIAA J.* 47 (10) (2009) 2391–2403.
[16] C. Bogey, C. Bailly, A family of low dispersive and low dissipative explicit schemes for flow and noise computations, *J. Comput. Phys.* 194 (1) (2004) 194–214.
[17] J. Berland, C. Bogey, O. Marsden, C. Bailly, High-order, low dispersive and low dissipative explicit schemes for multiple-scale and boundary problems, *J. Comput. Phys.* 224 (2) (2007) 637–662.
[18] C. Bogey, N. De Cacqueray, C. Bailly, A shock-capturing methodology based on adaptative spatial filtering for high-order non-linear computations, *J. Comput. Phys.* 228 (5) (2009) 1447–1465.
[19] J. Berland, C. Bogey, C. Bailly, Low-dissipation and low-dispersion fourth-order Runge–Kutta algorithm, *Comput. Fluids* 35 (2006) 1459–1463.
[20] C. Bogey, C. Bailly, Three-dimensional non-reflective boundary conditions for acoustic simulations: *far field formulation and validation test cases*, *Acta Acust. united Acust.* 88 (4) (2002) 463–471.
[21] S.W. Rienstra, Impedance models in time domain, including the extended Helmholtz resonator model, in: 12th AIAA/CEAS Aeroacoustics Conference, 8–10 May, Cambridge, MA, USA, AIAA Paper 2006-2686, 2006, pp. 1–20.
[22] D. Dragna, P. Blanc-Benon, Physically admissible impedance models for time-domain computations of outdoor sound propagation, *Acta Acust. united Acust.* 100 (3) (2014) 401–410.
[23] X.Y. Li, X.D. Li, C.K.W. Tam, Improved multipole broadband time-domain impedance boundary condition, *AIAA J.* 50 (4) (2012) 980–984.
[24] S. Busse-Gerstengarbe, C. Richter, F.H. Thiele, C. Lahiri, L. Enghardt, I. Roehle, P. Ferrante, A. Scofano, Impedance eduction based on microphone measurements of liners under grazing flow conditions, *AIAA J.* 50 (4) (2012) 867–879.
[25] Y. Özyörük, L.N. Long, A time-domain implementation of surface acoustic impedance condition with and without flow, *J. Comput. Acoust.* 5 (3) (1997) 277–296.
[26] K.-Y. Fung, H. Ju, Broadband time-domain impedance models, *AIAA J.* 39 (8) (2001) 1449–1454.
[27] D. Dragna, P. Pineau, P. Blanc-Benon, A generalized recursive convolution method for time-domain propagation in porous media, *J. Acoust. Soc. Am.* 138 (2) (2015) 1030–1042.
[28] R.M. Joseph, S.C. Hagness, A. Taflove, Direct time integration of Maxwell's equations in linear dispersive media with absorption for scattering and propagation of femtosecond electromagnetic pulses, *Opt. Lett.* 16 (18) (1991) 1412–1414.
[29] J. Bin, Y. Hussaini, S. Lee, Broadband impedance boundary conditions for the simulation of sound propagation in the time domain, *J. Acoust. Soc. Am.* 125 (2) (2009) 664–675.
[30] S. Zhong, X. Zhang, X. Huang, A controllable canonical form implementation of time domain impedance boundary conditions for broadband aeroacoustic computation, *J. Comput. Phys.* 313 (2016) 713–725.
[31] B. Gustavsen, A. Semlyen, Rational approximation of frequency domain responses by vector fitting, *IEEE Trans. Power Deliv.* 14 (3) (1999) 1052–1061.
[32] A.W. Guess, Calculation of perforated plate liner parameters from specified acoustic resistance and reactance, *J. Sound Vib.* 40 (1) (1975) 119–137.
[33] D. Burd, W. Eversman, J. Gallman, M. Drouin, Effects of two DOF lining tolerances on modeled inlet acoustic attenuation, in: 15th AIAA/CEAS Aeroacoustics Conference, 11–13 May, Miami, FL, USA, AIAA Paper 2009-3109, 2009, pp. 1–20.
[34] C. Othmani, T. Hentati, M. Taktak, T. Elnady, M. Haddar, Effect of liner characteristics on the acoustic performance of duct systems, *Arch. Acoust.* 40 (1) (2015) 117–127.
[35] B. Betgen, M.-A. Galland, E. Piot, F. Simon, Implementation and non-intrusive characterization of a hybrid active-passive liner with grazing flow, *Appl. Acoust.* 73 (6) (2012) 624–638.
[36] M. Escouflaire, Theoretical and numerical investigation of time-domain impedance models for computational aeroacoustics (Ph.D. thesis), Université du Maine, 2014.
[37] M. Bruneau, Fundamentals of acoustics, ISTE Ltd, London, UK, 2006, Eqs. (3.117) and (3.118), 145.
[38] T.J. Cox, P. D'antonio, *Acoustic Absorbers and Diffusers: Theory, Design and Application*, CRC Press, 2009.
[39] M.K. Myers, Transport of energy by disturbances in arbitrary steady flows, *J. Fluid Mech.* 226 (1991) 383–400.
[40] R.T. Marler, J.S. Arora, Survey of multi-objective optimization methods for engineering, *Struct. Multidiscip. Optim.* 26 (6) (2004) 369–395.
[41] K. Deb, A. Pratap, S. Agarwal, T. Meyarivan, A fast and elitist multiobjective genetic algorithm: *NSGA-II*, *IEEE Trans. Evol. Comput.* 6 (2) (2002) 182–197.
[42] E. Zio, R. Bazzo, A comparison of methods for selecting preferred solutions in multiobjective decision making, in: Computational Intelligence Systems in Industrial Engineering, Springer, 2012, pp. 23–43.
[43] M.O. Burak, M. Billson, L.-E. Eriksson, S. Baralon, Validation of a time-and frequency-domain grazing flow acoustic liner model, *AIAA J.* 47 (8) (2009) 1841–1848.
[44] G. Gabard, E. Brambley, A full discrete dispersion analysis of time-domain simulations of acoustic liners with flow, *J. Comput. Phys.* 273 (2014) 310–326.
[45] D. Vrajitoru, Large population or many generations for genetic algorithms? implications in information retrieval, in: Soft Computing in Information Retrieval, Springer, 2000, pp. 199–222.
[46] G. Gabard, Noise sources for duct acoustics simulations: *broadband noise and tones*, *AIAA J.* 52 (9) (2014) 1994–2006.